Tropical Cirrus in Global Storm-Resolving Models. Part II: Cirrus Life Cycle and Top-of-Atmosphere Radiative Fluxes

S. M. Turbeville[1], J. M. Nugent[1], T. P. Ackerman[1,2], C. S. Bretherton[1,3], and P. N. Blossey[1]

[1]Department of Atmospheric Sciences, University of Washington, Seattle, WA
[2]Joint Institute for the Study of the Atmosphere and Ocean, University of Washington, Seattle, WA
[3]Vulcan, Inc., Seattle, WA

Key Points:

- Statistics of tropical cirrus in 40-day high-resolution model simulations scatter around observational estimates
- The joint albedo-OLR histogram is a good observationally-testable diagnostic of cirrus life cycle
- Large differences between models are driven by ice microphysics and model dynamics

Corresponding author: S. M. Turbeville, smturbev@uw.edu

Abstract

Cirrus clouds of various thicknesses and radiative characteristics extend over much of the tropics, especially around deep convection. They can be difficult to observe due to their high altitude and sometimes small optical depths. They are also difficult to simulate in conventional global climate models, which have coarse grid spacings and simplified parameterizations of deep convection and cirrus formation. We investigate the representation of tropical cirrus in global storm-resolving models (GSRMs), which have higher spatial resolution and explicit convection and could more accurately represent cirrus cloud processes. This study uses GSRMs from the DYnamics of the Atmospheric general circulation Modeled On Non-hydrostatic Domains (DYAMOND) project. The aggregate life cycle of tropical cirrus is analyzed using joint albedo and outgoing longwave radiation (OLR) histograms to assess the fidelity of models in capturing the observed cirrus cloud populations over representative tropical ocean and land regions. The proportions of optically-thick deep convection, anvils, and cirrus vary across models and are reflected in the vertical distribution of cloud cover and top-of-atmosphere radiative fluxes. Model differences in cirrus populations, likely driven by subgrid processes such as ice microphysics, dominate over regional differences between convectively-active tropical land and ocean locations.

Plain Language Summary

Cirrus (ice) clouds vary in thickness and so have a wide range of impacts on Earth's energy budget. Unlike other clouds, thin cirrus reduce the amount of energy escaping to space, slightly warming the Earth. It is important to understand the differences in tropical cirrus cloud life cycles between models because tropical cirrus are a major source of uncertainty in the prediction of future climates. Cirrus clouds cover a large area in space and can last up to several days, yet they are difficult to measure with satellites and ground-based instruments. We instead use computer models to simulate tropical cirrus, specifically global storm-resolving models (GSRMs) which are able provide a level of detail not possible through observations. Unfortunately, most models have large biases in cloud properties. These differences arise from the imperfect representation of ice in the models. Our goal is to understand the model differences in representation of ice clouds using statistical analysis of the life cycle of cirrus in each model.

1 Introduction

High clouds in the tropics have been difficult to reproduce in global climate models (GCMs) because of their complex microphysics and radiative properties (e.g., Del Genio, 2012; Stephens, 2005). Proper representation of the properties of tropical cirrus, especially cloud amount and hydrometeor distribution, is a key issue for improving GCMs (Inoue et al., 2010). GCMs generally have a low spatial resolution, which is unable to explicitly represent convection and the subsequent tropical cloud life cycle. Diverse convective and ice microphysical parameterizations lead to large differences between GCMs in the ice cloud population (Del Genio, 2012).

This is the second of two papers comparing the formation and properties of tropical cirrus in relation to deep convection in several high-resolution global storm-resolving models (GSRMs). Nugent et al. (2021) (hereafter Part I) focuses on deep convection and its role as a source of ice and vapor for cirrus formation. Here, we compare the simulated ice cloud populations with satellite observations, interpreting them in terms of an aggregate cirrus life cycle.

As noted in Part I, GSRMs are attractive for modeling tropical cirrus. Unlike conventional climate models with horizontal grid spacings of 25–200 km, GSRMs have sub-5 km grid spacing that enables them to explicitly simulate deep convection and its detrainment

of ice into the upper troposphere and better represent the mesoscale gravity wave spectrum and orographic features. Therefore, GSRMs have the potential to act as a better surrogate for the real atmosphere to study scientific questions about tropical cloud populations and the aggregate life cycle of tropical cirrus, including how they might respond to climate change. However, before we can use GSRMs to try to answer such questions, we must evaluate their performance compared to available observations.

We focus on three contrasting $10^\circ \times 10^\circ$ regions in or near frequent deep convection during the simulated period of 1 August–10 September 2016. The first two regions were also used in Part I. Our main focus of analysis is a tropical West Pacific (TWP) region centered near Manus, Papua New Guinea. The second region, which sampled continental convection, is centered over the Sahel (SHL) in west Africa. We added a third region (NAU) centered near Nauru Island on the edge of the Pacific warm pool, where cirrus are often thinner and have originated from remote convection.

1.1 Archetypal Life Cycle of Tropical Cirrus

Convection plays a significant role in the formation and composition of tropical cirrus clouds (Fueglistaler et al., 2009). Houze (1981) describes the idealized life cycle of a typical tropical mesoscale convective system, which begins with a narrow core of deep convection in the formation stage that then matures and spreads into a system with stratiform precipitation and cirrus outflow. As the system weakens, the stratiform precipitation persists but tends not to reach the ground. Finally, the upper-level cirrus clouds break up and thin in the dissipating stage (Houze, 1981). During this evolution, the cloud system has notably different effects on the reflected shortwave (RSW) and outgoing longwave radiation (OLR) at the top of atmosphere (TOA) due to the changing amount of liquid and ice in the vertical column and the change in the associated optical depth.

We focus on the radiative impacts of the life cycle through the populations of thick, medium, and thin clouds and their relative cloud radiative effects. Following Hartmann and Short (1980), we use joint albedo-OLR histograms to characterize and compare cloud populations and their TOA radiative effects in models and satellite observations. These histograms do not follow individual cloud systems, but can be interpreted as proxies for the cirrus life cycle. As tropical cirrus clouds evolve from thick to thin, they tend to follow a characteristic path in the albedo-OLR plane associated with cooling to warming cloud radiative effects (CRE), switching signs for an ice water path (IWP) around 200 g m^{-2}, (Berry & Mace, 2014) that can be qualitatively reproduced in cloud-resolving simulations (Gasparini et al., 2019).

The overall radiative properties of tropical cloud fields integrate over all phases of the cirrus life cycle to be approximately neutral in the TWP. This observed cancellation of longwave (LW) and shortwave (SW) CRE in the TWP has been well documented, but whether it is coincidental or reflects some deeper physical regulating principle is still controversial (e.g., Ramanathan et al., 1989; Hartmann et al., 2001; Kiehl, 1994). Ackerman et al. (1988) showed that cirrus with an optical depth less than $\sim$5 have a net warming effect since they absorb LW radiation more than they reflect SW solar radiation at TOA. Conversely, thick anvils and deep convective clouds reflect SW radiation more than they absorb LW radiation, resulting in a net cooling effect. In the TWP and NAU, the large negative CRE from relatively infrequent deep convective events is nearly offset by the widespread, thin cirrus clouds with slightly positive CRE (Wall et al., 2018). In this study, we analyze whether GSRMs capture this observed neutrality in the TWP and NAU regions.

We also investigate the representation of cirrus in the tropical tropopause layer (TTL), a transitional layer from troposphere to stratosphere defined as in Part I to extend from 14–18 km altitude. TTL cirrus are the highest clouds in the tropics and are thought to play an active role in the thermodynamic structure of this layer and in setting lower-stratospheric water vapor concentrations.

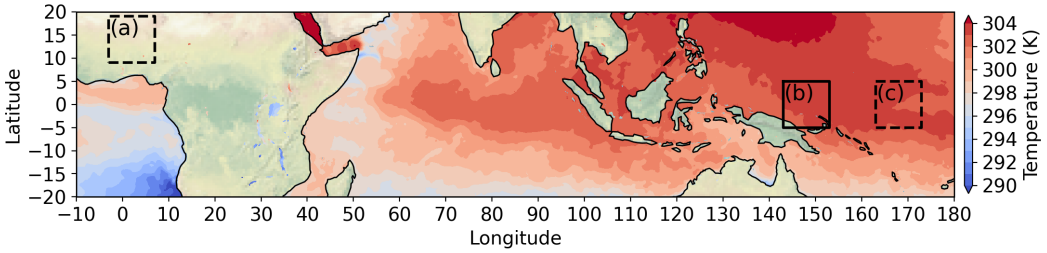

Figure 1. The three analysis regions: (a) the Sahel (SHL; 3°W–7°E, 9°N–19°N), (b) Manus, Papua New Guinea (TWP; 143°E–153°E, 5°N–5°S), and (c) Nauru Island (NAU; 163°E–173°E, 5°N–5°S). Shading shows ERA5 sea surface temperatures on 1 August 2016.

In section 2, we review data sources reused from Part I and introduce new data and analysis methods. Results for the TWP region are presented in section 3 and compared across regions in section 4. We analyze TTL cirrus simulated by the GSRMs in section 5. Section 6 presents our conclusions.

2 Methods and Data

The focus of this paper is comparing the population and implied life cycle of cirrus in GSRMs vs. satellite observations, in different parts of the tropics, with a focus on their TOA radiative properties.

The GSRM radiative transfer schemes operate on individual grid columns for computational efficiency. Consequently, our analysis largely focuses on column-by-column statistics, not horizontal relationships between columns. Properties of GSRM grid columns that we will compare with observations include OLR, albedo, ice water content, and frozen water path.

In this section, we describe the study domains, models, and data used. The models and some data are described in more detail in Part I, so we only elaborate on our new data sources and analysis methods.

2.1 Study Domains

The global simulations and observational data are studied in three contrasting $10° \times 10°$ latitude-longitude regions across the tropics shown in Figure 1. These three regions each contain a substantial but manageable volume of model output (at least 66,000 grid columns). Two of these regions are used in Part I: (a) the Sahel (SHL) in west Africa, representative of continental deep convection, and (b) the TWP region near Manus Island, Papua New Guinea, representative of warm oceanic deep convection, which will be our primary focus. We add (c) a secondary region in the west Pacific near Nauru Island (NAU), in which there is less local deep convection, so more of the cirrus has aged. Each region at some time included an observational Department of Energy Atmospheric Radiation Measurement site offering a comprehensive set of ground-based observations for future work.

The three study regions experienced typical amounts of precipitation over the simulated period in August and early September 2016, with a weak MJO in mid-August and slight La Niña conditions. This justifies comparing model output with climatological observations from the same season in other years.

2.2 The DYAMOND GSRMs

Like Part I, this study uses outputs from GSRMs that participated in the DYnamics of the Atmosphere general circulation Modeled On Non-hydrostatic Domains (DYAMOND) intercomparison project. The DYAMOND project compared free-running GSRMs over the 40-day period from 00 UTC 1 August to 00 UTC 11 September 2016, initialized from ERA5 reanalysis, with the sea surface temperature evolution also based on ERA5. As noted in Part I, the DYAMOND GSRMs use diverse choices of ice microphysics, advection schemes, etc. However, because of their fine grid, they do not use deep convection parameterizations, allowing the detrainment of ice into the tropical upper troposphere to be explicitly simulated. Thus, it is interesting to compare their simulated populations of tropical cirrus clouds. Because the GSRMs are free-running, we compare the model output statistically rather than comparing specific weather systems. We disregard the first two days of model output for all models as a spin-up period for cloud processes.

We focus on four models: NICAM, FV3, ICON, and SAM (collectively referred to as NFIS) because those models provide sufficient output to compute the total IWP and also include 3D output for cloud ice (see Table 1). For more information, see section 2.1 of Part I.

Table 1. List of DYAMOND GSRMs used in this study by their acronym, horizontal grid spacing, and availability of ice/snow/graupel for 3D water content (WC) and 2D integrated water path (WP).

	Grid	3D WC			2D WP		
Model	spacing	I	S	G	I	S	G
NICAM	3.5 km	X	X	X	X	X	X
FV3	3.25 km	X			X	X	X
ICON	2.5 km	X			X	X	X
SAM	4 km	X			X	X	X
ARPNH*	2.5 km				X		
IFS*	4 km				X	X	-
MPAS*	3.5 km				X	X	X
UM*	7.8 km				X		

* Coarsened model output with 0.1° resolution used
\- Graupel not included in microphysics scheme

The DYAMOND models output 2D fields, such as precipitation, available integrated water paths (listed in Table 1), and SW and LW fluxes at TOA, at 15 minute intervals. Some 2D comparisons are based on output coarsened to a $0.1^\circ \times 0.1^\circ$ grid in all models. We also use 3-hourly 3D output of temperature, hydrometeor mixing ratios (available frozen hydrometeors listed in Table 1), specific humidity, vertical velocity, pressure, and height. The vertical grid spacings are similar between models. For example, NICAM has 10 vertical levels within the 14–18 km TTL, while FV3, ICON, and SAM all have 8 vertical levels in the TTL.

Figure 2 shows a typical snapshot of total water content from FV3 in a $10^\circ \times 10^\circ$ latitude-longitude area for the TWP. Darker shading indicates more ice mass in a particular grid cell. Figure 2 demonstrates the detail and complexity of simulated cloud systems afforded by the high resolution. Some convective cores are surrounded by anvil outflow and thinner cirrus with underlying low clouds.

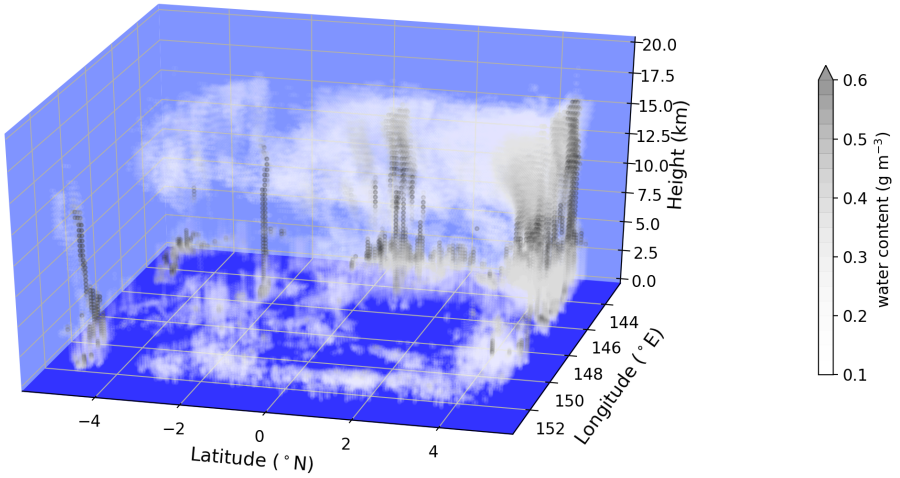

Figure 2. Snapshot of cloud ice water content (g m^{-3}) in FV3 at 6:00 UTC on 3 August 2016 for the 10° × 10° TWP study region.

2.3 Data

The CALIPSO-CloudSat-CERES-MODIS (CCCM) merged product and the raDAR-liDAR (DARDAR) product are reused from Part I. In addition, this paper uses TOA radiative fluxes from the CERES SYN1 deg product.

CCCM provides collocated cloud microphysics and TOA radiative fluxes with a horizontal footprint of roughly 30 km (Kato et al., 2011). We use daytime values from this dataset (13:30 local time) when albedo can be measured and seasonally subset to July–September 2007–2010.

DARDAR combines CloudSat, CALIPSO, and MODIS satellite measurements to derive microphysical properties of cirrus clouds over a broad range of optical thicknesses (Deng et al., 2013; Sokol & Hartmann, 2020) with a fine horizontal spacing of ∼1.1 km and a vertical resolution of 60 m. DARDAR has a higher retrieval uncertainty for optically thin cirrus layers, which are visible with only the lidar (Cazenave et al., 2019). We use both daytime and nighttime values from the 2009 July-August-September data. For both TWP and NAU, there was approximately 50% more precipitation in August 2009 compared to August 2016 according to ECMWF reanalysis; this should be kept in mind when comparing DARDAR to the DYAMOND output in these regions.

We use OLR and RSW radiation from the CERES SYN1 product, available from 2000–2019. CERES SYN1 data have a 1° × 1° horizontal resolution with an approximate uncertainty of 3 W m^{-2} (Kato et al., 2018). We seasonally subset this data to 1 August to 10 September of each year.

For comparisons between GSRM output and these observations, we coarsen the model output to 0.3° × 0.3° to match CCCM or 1° × 1° to match CERES. The GSRM output is not coarsened for comparisons with DARDAR, which has a similar footprint to the model grid spacings.

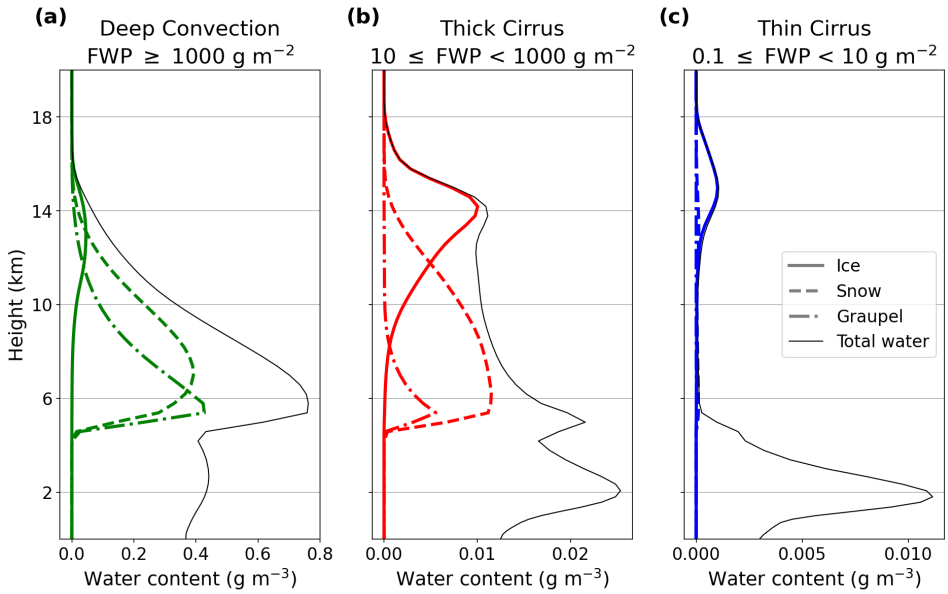

Figure 3. Vertical profiles of water content (g m^{-3}) for NICAM showing the breakdown between ice (solid), snow (dashed), and graupel (dot-dashed) in areas of (a) deep convection (green), (b) thick cirrus (red), and (c) thin cirrus (blue). The total water content, including liquid, is shown in the thin black line. The x-axis is different for each plot.

2.4 FWP Categorization

We classify each grid column according to its column-integrated frozen water path (FWP), defined as the sum of ice, snow, and graupel water paths. As in section 2.5 of Part I, we define three thickness categories that approximately correspond to (1) deep convection, (2) thick cirrus, and (3) thin cirrus:

FWP Categories:				
CAT 1	Deep convection		FWP	≥ 1000 g m^{-2}
CAT 2	Thick cirrus	$10 \leq$	FWP	< 1000 g m^{-2}
CAT 3	Thin cirrus	$0.1 \leq$	FWP	< 10 g m^{-2}
	Cirrus-free		FWP	< 0.1 g m^{-2}

For comparisons to observational data and previous studies, we use the model output of hydrometeor mixing ratios to calculate IWC and frozen water content (FWC) where possible as well as liquid water content (LWC). For FV3, ICON, and SAM, only cloud ice and cloud water were saved for the 3D hydrometeors, so we can only calculate the FWC for NICAM. We show vertical profiles of cloud ice, snow, and graupel in NICAM in Figure 3 to demonstrate how FWC differs between cloud types. Snow and graupel in NICAM make up the bulk of frozen mass below the TTL and a small, but non-negligible, portion of the total frozen water in the upper troposphere in the rare columns with vigorous deep convection (Figure 3a). Columns with thick cirrus in NICAM have snow and graupel dominant below and ice dominant above 12.5 km (Figure 3b). Thin cirrus are made mostly of cloud ice with a negligible amount of snow or graupel. We therefore assume the IWC is a decent representation of FWC above 12.5 km for thin cirrus, but underestimates FWC in deep convection or anvils in models that do not output 3D snow or graupel.

2.5 Clear Sky Thresholds

The DYAMOND models produce few columns that are truly ice-free. The model microphysics schemes typically retain small amounts of FWC. FWCs below 5×10^{-4} g m^{-3} are difficult to detect from aircraft or satellite data (Deng et al., 2013). Therefore, we adopt this value as a 'clear-sky' or 'cirrus-free' threshold for simulated IWC. The frequency of thin cirrus clouds is sensitive to this threshold in all of the models.

Given this threshold and assuming a GSRM vertical grid spacing of 200 m, the column-integrated cloud ice water path must exceed 0.1 g m^{-2} for the volume to be considered cloudy, so this is chosen as our cirrus-free FWP threshold. DARDAR does not retrieve FWP values less than 0.1 g m^{-2}.

3 The Aggregate Life Cycle of Tropical Cirrus in the TWP

In this section, we determine the cloud populations from the albedo-OLR histograms and compare the radiative climatologies in each model to satellite observations. Then, the life cycle of tropical cirrus is quantified using FWP categories for the NFIS models in the TWP. The vertical structure and ice properties of clouds in the TWP are used to explain the differences in cloud populations between models. Our analysis relies on statistical aggregates from snapshots of cloud properties and their corresponding radiative fluxes.

3.1 Cloud Populations

A joint albedo-OLR histogram gives a useful summary of how the cloud populations relate to the TOA radiation budget (Hartmann & Short, 1980). Over ocean, the albedo can be regarded as a proxy for cloud optical depth. The OLR is an indicator of cloud-top height; thus, we can differentiate between cloud types with these two 2D variables. Using albedo restricts our analysis of the models to mid-day (10 am–2 pm local time) to eliminate any anomalies occurring near dawn and dusk. The model outputs are coarsened to match the 30 km CCCM footprint.

Figure 4 compares simulated albedo-OLR histograms for the TWP during 1 August–10 September 2016 (DYAMOND GSRMs) and July-August-September 2007–2010 (CCCM observations). The observations are shown in Figure 4a. The distribution also encompasses a banana-shaped curve extending from a maximum probability density at the clear-sky values in the lower right up to a secondary deep convective peak at high albedo and low OLR. There is also a slight shoulder of moderate albedo and high OLR occurrences.

Figure 4f interprets this joint histogram in terms of component cloud types. A typical tropical cirrus life cycle roughly aligns with the black arrow in Figure 4f, starting with deep convection then progressing through thick and then thin cirrus. The light blue ellipse indicates a population of low, liquid-dominated clouds with tops below 8 km. These can induce relatively strong albedo perturbations with less impact on OLR than deep convective cloud systems. The orange circle demarcates clear sky. These cloud types may shift somewhat in albedo-OLR space in other convectively-active regions of the tropics with different surface albedo and humidity/temperature profiles.

In comparing the TWP albedo-OLR histograms for each model (Figure 4b–e,g–j), we look for three characteristic properties of the observations: (1) a clear sky peak, (2) a secondary peak in deep convection, and (3) a banana-shaped distribution. All of the models successfully capture the high OLR-low albedo clear-sky peak, though FV3, ICON, and IFS have slightly higher clear-sky OLR values. FV3, MPAS, and UM also capture the local maximum corresponding to observed deep convective radiative characteristics. NICAM and IFS match the general banana shape of the histogram very well but do not capture the secondary deep convective peak. ICON, SAM, and ARPNH all fail to simulate the secondary deep convective peak and do not match the banana-shaped distribution of the

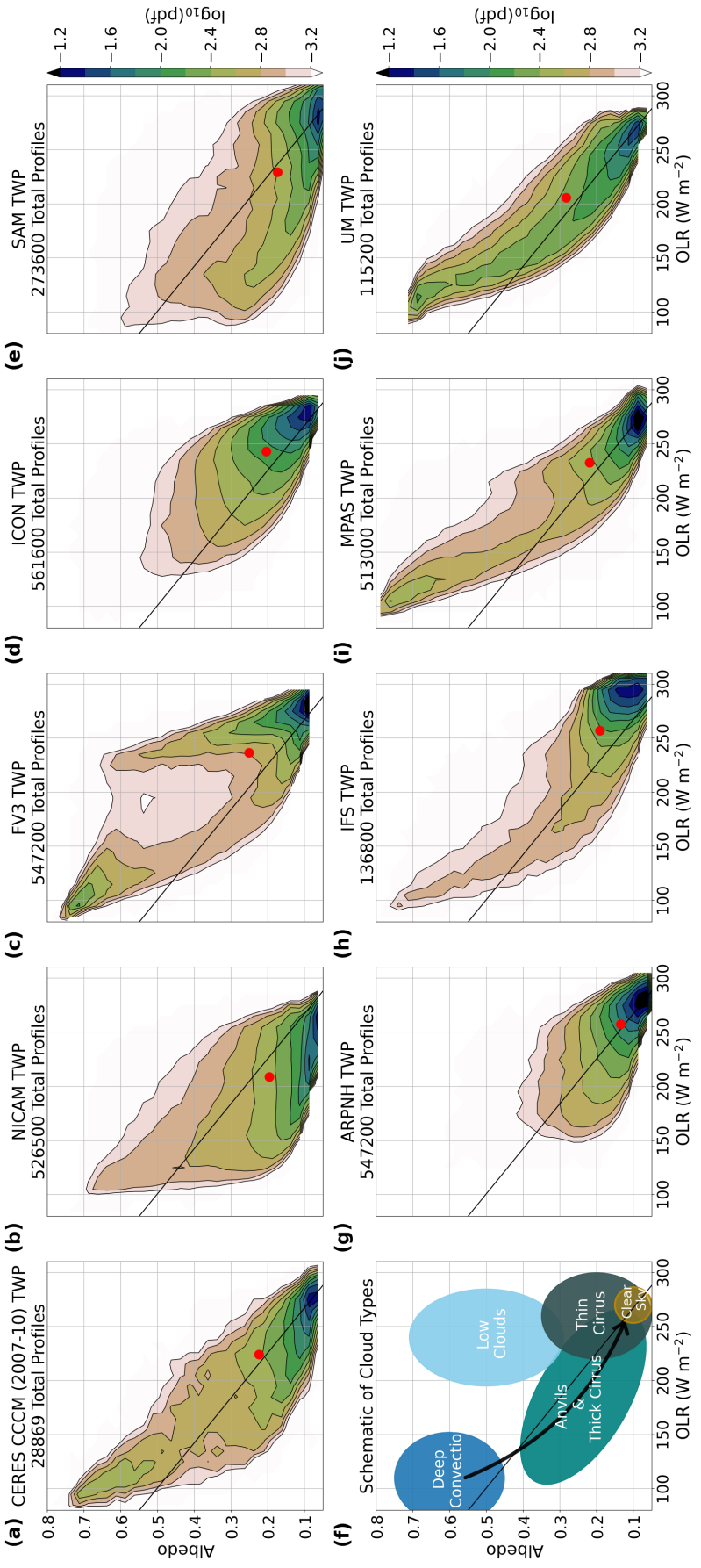

Figure 4. Density plot of albedo and OLR for (a) CCCM and (b–e,g–j) the DYAMOND models for days 3–40. The schematic of cloud types is reproduced in (f). Model output averaged over 0.3° to match the CCCM footprint. There are 32 and 27 evenly spaced bins for the OLR and albedo, respectively (as in Gasparini et al., 2019). The red dot indicates the mean albedo-OLR pairing for the distribution. Neutral CRE is calculated from observation as the black line.

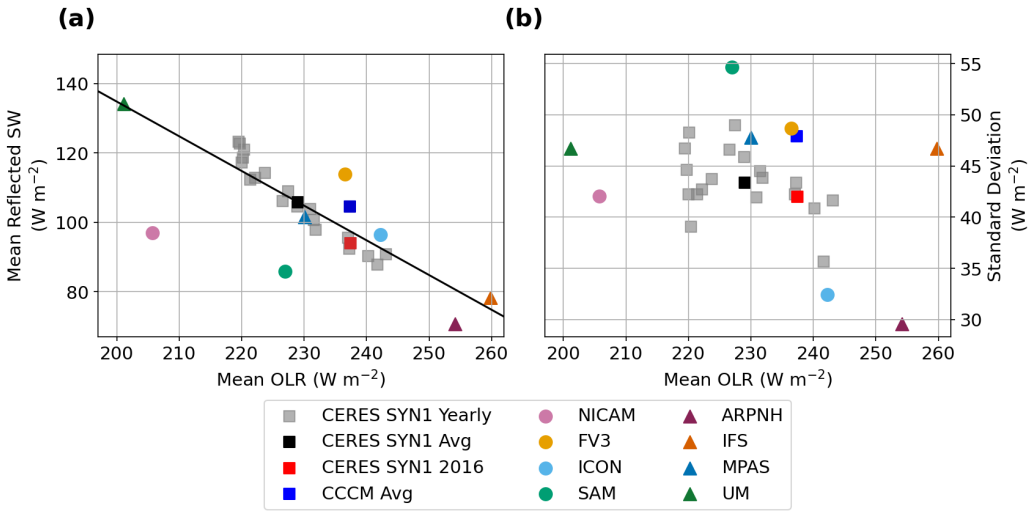

Figure 5. (a) Mean OLR plotted against mean reflected SW radiation at TOA from days 3–40. The linear fit of CERES SYN1 is plotted as the black line. (b) Daily mean versus standard deviation of OLR. Before computing the standard deviation, the OLR from each model was coarsened to match the hourly and $1^\circ \times 1^\circ$ horizontal resolution of CERES SYN1.

observations. ICON and ARPNH do not have albedo-OLR values characteristic of deep convection because their deep convective cores are not surrounded by sufficient thick, cold anvil within the CCCM footprint. SAM has convection reaching the upper troposphere, shown by the low OLR values, but the associated cloud is optically too thin to match the observed deep convective characteristics. FV3 has a distinct population of liquid-dominated clouds reaching high albedo values despite relatively high OLR.

In summary, MPAS and UM capture all of the key characteristics observed in the TWP. NICAM, FV3, and IFS also capture most key traits of cloud populations in the TWP, while ICON, SAM, and ARPNH deviate greatly from the observed cloud populations.

3.2 TOA Radiation Balance and CRE

The TWP-mean albedo and OLR (the red dot in each panel of Figure 4) can be inferred by averaging over the albedo-OLR histogram. The GSRMs scatter around the observed albedo of 0.22, with albedos ranging from 0.14 (ARPNH) to 0.3 (UM). They similarly scatter about the observed OLR of 225 W m^{-2}, from 205 W m^{-2} (NICAM) to 255 W m^{-2} (ARPNH). Some of this scatter comes from different characteristic clear-sky albedo and OLR, but most of it is due to the different simulated cloud populations.

Hartmann et al. (2001) noted a characteristic of the TWP cloud population–near zero net cloud radiative effect (CRE, defined as the cloud-induced change in the net TOA radiation). This is due to a balance between thick convective and cirrus clouds, which increase RSW more than they decrease OLR, and thin cirrus, which do the opposite. The black neutral-CRE line in all of the panels of Figure 4 shows the albedos and OLRs for which this balance would occur in the observations. It is computed by locating the clear-sky occurrence peaks of OLR and albedo in the CCCM data. The longwave CRE is calculated as the difference between the estimated clear-sky OLR and the actual OLR. while the shortwave CRE (which is negative) is calculated as the difference between the clear-sky albedo and

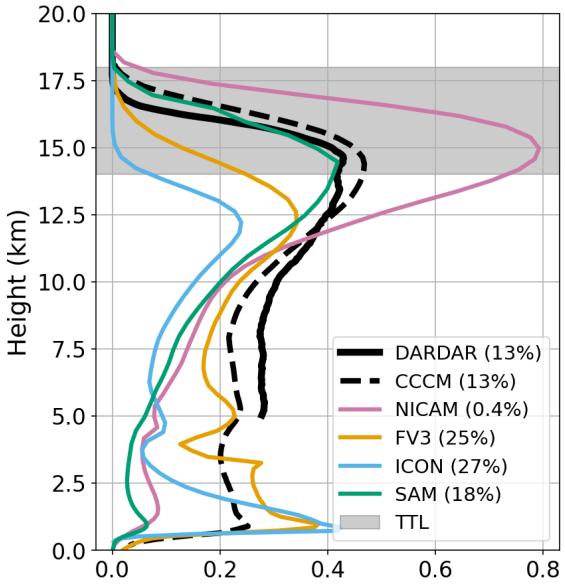

Figure 6. Vertical occurrence of clouds for each model from days 3–40 compared to observations from DARDAR and CCCM. For the models, only cloud ice is used to calculate cloud fraction; the observations implicitly include all frozen hydrometeors.

the actual albedo, multiplied by the daily-mean insolation at the given location and season (413.2 W m^{-2} in the TWP and NAU regions and 435.3 W m^{-2} in the SHL region).

The red dot in the CCCM panel almost overlays this black line, showing the net neutrality of CRE in the TWP. For the model panels, a red dot above (below) the black line signifies the clouds contribute an overall radiative cooling (warming) effect. The models approximate the observed CRE neutrality to within 30 W m^{-2}. Only NICAM simulates substantial positive net CRE (cloud-radiative warming). The black line corresponds to a constant total outgoing radiative flux (LW+SW) equal to the 3-year mean. The model variability mostly scatters $\pm$10 W m^{-2} around the 3-year mean along the black line, which also is approximately a line of CRE neutrality.

We include CCCM and CERES SYN1 satellite retrievals of TOA radiative fluxes in Figure 5. Since the CERES SYN1 observations span 20 years of 40-day periods and the GSRM simulations span 1 year for 40 days, we can assess whether the GSRM results are within the range of interannual variability of TOA radiative fluxes. The model spread should ideally be contained within this range of natural annual variability. That is true for MPAS, FV3, and ICON, but not for the other models (Figure 5a). Some of those models near CRE neutrality (SAM and ICON in Figure 4) lie outside the observed interannual range (Figure 5). Extreme examples of this are UM and IFS, which each had biases of $\sim$30 W m^{-2} in OLR (high in IFS, low in UM) with offsetting biases in reflected SW. These two models match the banana shape of the observed albedo-OLR distribution in Figure 4, but their frequency of occurrence at the two ends of the banana are biased, with IFS tending to produce near clear-sky values and UM tending towards thick anvils. Other models, especially NICAM, lie far from CRE neutrality so as to be inconsistent with observations from any year.

3.3 Sources of GSRM TOA Radiation Bias

As a group, the models capture key observed radiative characteristics of the cloud populations. However, the albedo-OLR histograms show that individual GSRMs simulate clouds differently from each other and the observations. How do these differences arise? Two potential contributors are the vertical profile of fractional coverage and the thickness of clouds, as measured by their frozen water path.

Observed vertical profiles of cloud fraction in convectively active regions of the tropics have their largest peak in the upper troposphere (Hollars et al., 2004), where it is associated with cirrus clouds. Different GSRMs simulate different cirrus cloud-top heights, likely due to their formulations of ice microphysics and dynamics. Virts et al. (2010) show that the fractional coverage of upper troposphere cirrus maximizes in the 14–15 km layer, which corresponds to the base of the TTL. Figure 6 compares observational estimates of vertically-resolved cloud fraction from DARDAR (solid) and CCCM (dashed) with the NFIS GSRMs in the TWP. The cloud fraction peaks near 15 km in NICAM and SAM, consistent with these observations, but peaks well below the TTL in FV3 and ICON at $\sim$12.5 km.

NICAM has too much cloud cover in the upper troposphere and TTL but too few low clouds when compared to DARDAR and CCCM. This contributes to its low bias in OLR. FV3 has too few upper-level clouds and too many low clouds; this leads to a high bias in RSW. ICON has too many low clouds but too few ice clouds everywhere above 2 km altitude, also leading to a high bias in OLR. SAM is reasonably close in frequency and shape to the observed cirrus cloud occurrence, but has too little low cloud, leading to a low bias in RSW. Part I shows that the upper level cloud occurrence in the NFIS models approximately tracks their relative humidity profiles (Figure 2b, d in Part I).

3.4 Frozen Water Path Distribution

We investigate the characteristics of ice clouds in each model more closely through the distribution of frozen mass in each column over the August–September period. We further break down the ice into three main categories that roughly align with the deep convection, thick cirrus, and thin cirrus regimes in the albedo-OLR diagram shown in Figure 4f (schematic). Because the FWP also influences both the SW and LW radiative characteristics of the cirrus, this analysis can also shed further light on GSRM cloud-radiative biases; that will be addressed in the following section. We ignore LWP in this categorization since our focus is on cirrus clouds. This categorization is done at the full model resolution, since that is comparable to that of the DARDAR FWP observations.

Figure 7 shows FWP histograms for DARDAR and the four NFIS models. The FWP categories are plotted as different colors corresponding to deep convection (CAT 1; green), thick cirrus (CAT 2; red), thin cirrus (CAT 3; blue), and cirrus-free (gray).

Deep convection occupies 11% of all columns in space and time in the DARDAR observations, and 3–5% in the models. The DARDAR measurements were taken during an August with nearly 50% more convection than August 2016. This suggests an observationally-based estimate for 2016 of 7% occurrence of CAT 1. The DARDAR methodology may not accurately retrieve FWP in deep convective columns dominated by snow and graupel, so the remaining difference in CAT 1 frequency between the models and observations may not be meaningful.

Thick cirrus occupy the most area in space and time, 48% for DARDAR and 30–67% for the models. Thin cirrus occurs slightly less often, 25% for DARDAR and 28–38% for the GSRMs. Lastly, the cirrus-free category, occupying 16% fractional area in DARDAR, has a broad range of 1–32% across the models. Berry and Mace (2014) find that the CRE transitions from cooling to warming as FWP decreases to ∼200 g m^{-2}. This transition occurs in CAT 2; subsequently, CAT 2 has the strongest influence on the overall cloud radiative effect in the region. The models range from cooling in FV3 to warming in NICAM.

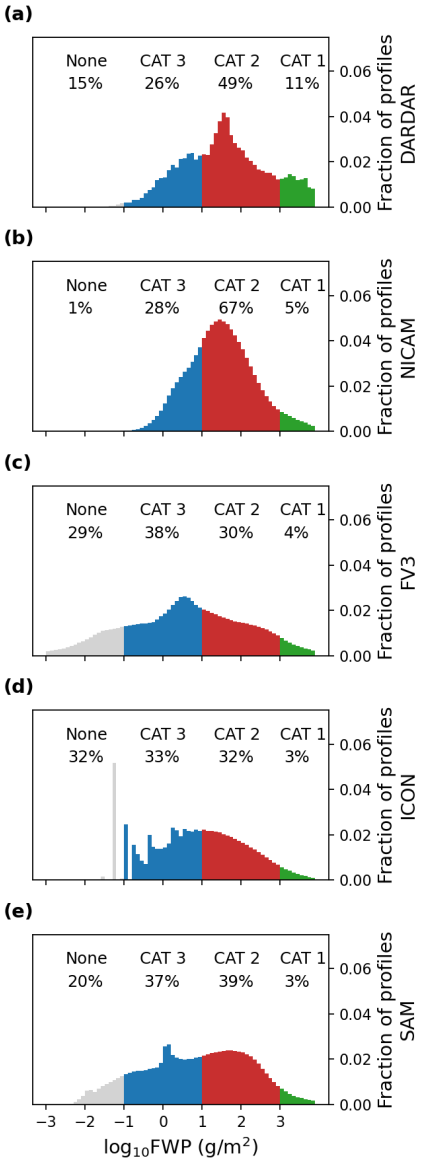

Figure 7. Total column FWP for observations from (a) DARDAR and model output from days 3–40 for (b) NICAM, (c) FV3, (d) ICON, and (e) SAM colored by the FWP categories: (green) deep convection, (red) thick cirrus, and (blue) thin cirrus.

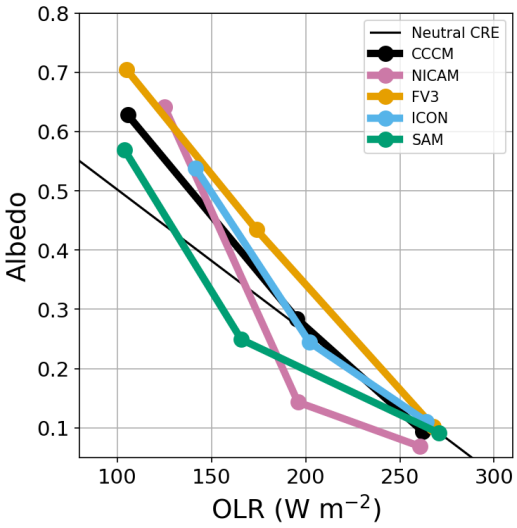

Figure 8. The median albedo-OLR pairing for each category is plotted as closed circles for the data and models. Models are not coarsened to match the CCCM footprint. CAT 1 is the upper-leftmost point and is connected to CAT 2 and then CAT 3 by straight lines, signifying the aggregate life cycle of tropical cirrus.

There is a large range of FWP histogram shapes among the models. NICAM most closely matches the shape of DARDAR including the peak FWP near 30 g m^{-2}, but has almost no cirrus-free columns. FV3 and ICON peak at a smaller FWP while SAM peaks at a larger FWP.

Our results confirm the spatial dominance of the maturing and dissipating stages of the ideal life cycle from Houze (1981). The model FWP distributions are diverse, presumably reflecting differences in their ice microphysics schemes and perhaps also their model dynamics. As a group, the FWP distributions tend to scatter around the DARDAR observations in both modal value and category frequency.

3.5 FWP as a Control on Albedo and OLR

To what extent do intermodel differences in the FWP histogram correlate with their differences in albedo-OLR histograms and in TOA radiative fluxes seen in Figure 4? Binning the albedo-OLR diagrams into FWP categories helps address this question, while allowing us to construct a simple aggregate radiative description of the cirrus life cycle for each NFIS model and the observations.

In Figure 8, the median value of OLR and albedo for each FWP category is plotted, with CAT 1 deep convection in the upper left corner progressing through anvils to CAT 2 thick cirrus and ending with CAT 3 thin cirrus in the lower right. Each model traces a unique path from one category to the next in the albedo-OLR plane. The median values are used because Berry and Mace (2014) found that the mean value of IWP is a poor diagnostic of radiative properties of tropical cirrus, and because the mean values of albedo are dominated by high-albedo liquid clouds, while our focus is on ice clouds. The GSRMs are analyzed at their fine native grid resolution to allow better FWP sorting, so the observations have a footprint about 6X larger in each direction than the models. To partly compensate, the CCCM FWP is calculated only for the cloudy fraction of the footprint.

Category 1 covers only a small fractional area, especially in the models, but is of particular interest since deep convection is important for bringing ice into the TTL (Part I) that may also affect the thick and thin cirrus categories. Figure 8 shows that FV3 and SAM have the lowest median OLR for CAT 1, comparable to the CCCM observations, meaning that they produce tall convective towers with the coldest cloud tops, even though NICAM has more high cold cirrus overall. Despite its low OLR, SAM has a slightly lower albedo than FV3, NICAM, or the observations, indicating that its convective clouds are not as optically thick. ICON has the highest OLR and lowest albedo, meaning it does not have convective towers that reach as high or are as reflective as the other models.

The largest differences between models occur in CAT 2, with OLR ranging from 156–202 W m^{-2} and albedo from 0.15–0.44. This category covers much of the TWP area, so these differences are predictive of area-mean net CRE. The net CRE in CAT 2 is most positive (warming) for NICAM, followed by SAM, with slight negative CAT 2 CRE for ICON and more negative CAT 2 CRE for FV3. This is exactly the same ordering seen for area-mean CRE in Figure 5a.

The NFIS models have much more similar median albedo and OLR for Category 3 (thin cirrus), which has relatively weak radiative effects. Thus, thin cirrus are comparatively unimportant to intermodel differences in area-mean net CRE over the TWP.

Even with FWP fixed, a major factor affecting albedo is the presence of liquid clouds, because they are more reflective than ice clouds. FV3 tends to have some liquid clouds underlying CAT 2 and 3 cirrus. ICON tends to have more liquid clouds underlying CAT 3 cirrus clouds.

4 Regional Comparison

Here, we compare results from the TWP with our two other tropical study regions described in section 2.1, SHL (land convection) and NAU (on the edge of an active ocean convection region), to see how the NFIS models simulate cirrus in these different yet climatically significant regions.

4.1 Cloud Populations

The SHL has a much brighter surface than the dark ocean. The northern half of the SHL region is the high-albedo Sahara while the southern half has more vegetation and a lower surface albedo. This causes a larger variation within the region in clear-sky albedo and OLR values and a higher albedo overall than the ocean, both in the CCCM observations and in the four NFIS GSRMs (see Figure 9a–e). Most clouds lie below the CCCM-based line of neutral CRE in the SHL (Figure 9a), implying a stronger warming effect of clouds over the SHL and/or a GSRM with a lower surface albedo than that inferred from the CCCM observations. CCCM data also have fewer deep convective columns with high albedo and low OLR in SHL than the TWP. This cloud distribution reflects more sporadic deep convection in a drier environment. Qualitatively, all four GSRMs also show this pattern.

Compared to the TWP, NAU has fewer deep convective columns and no secondary peak at low OLR-high albedo values. The mean albedo-OLR pair (red dot in Figure 9k) in NAU is slightly above the line of neutral CRE, signifying a small net cloud cooling effect. This cooling is likely due to the larger population of low clouds, which are more reflective than extended cirrus clouds. The four GSRMs all simulate the weakening of the deep convective peak, but only SAM shows an enhanced shallow-cloud peak of higher albedo and high OLR at NAU compared to TWP (Figure 9l–o).

Many biases of individual GSRMs identified in the TWP persist across regions. For example, NICAM has frequent thin cirrus, FV3 has a large liquid cloud population, and ICON and SAM do not have sufficient deep convection (Figure 9).

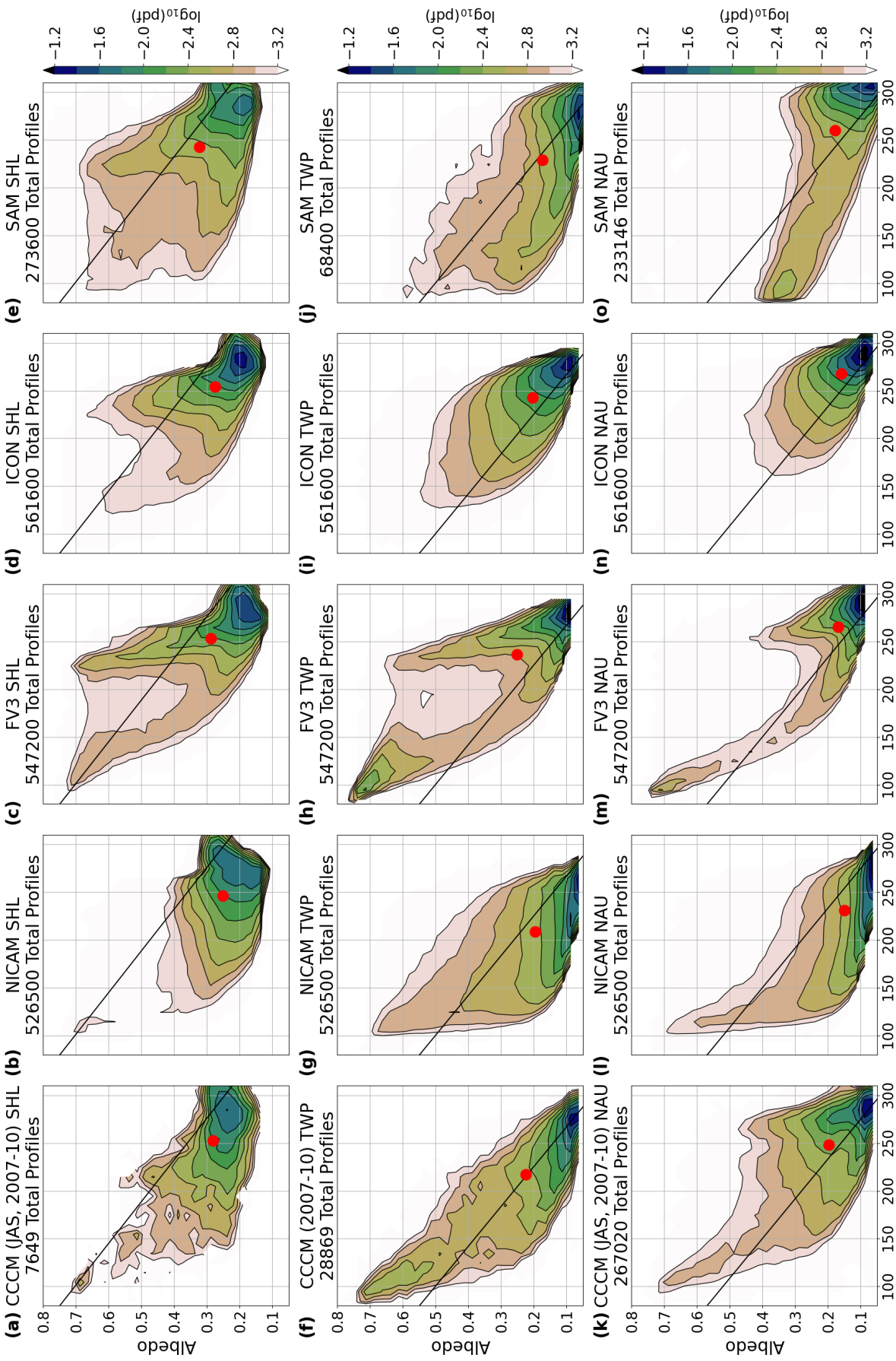

Figure 9. Joint albedo-OLR histograms for SHL (a–e), TWP (f-j), and NAU (k–o) for (a, f, k) the observations from CCCM and the model output from (b, g, l) NICAM, (c, h, m) FV3, (d, i, n) ICON, and (e, j, o) SAM. The black line of neutral CRE was calculated for each region from the observations.

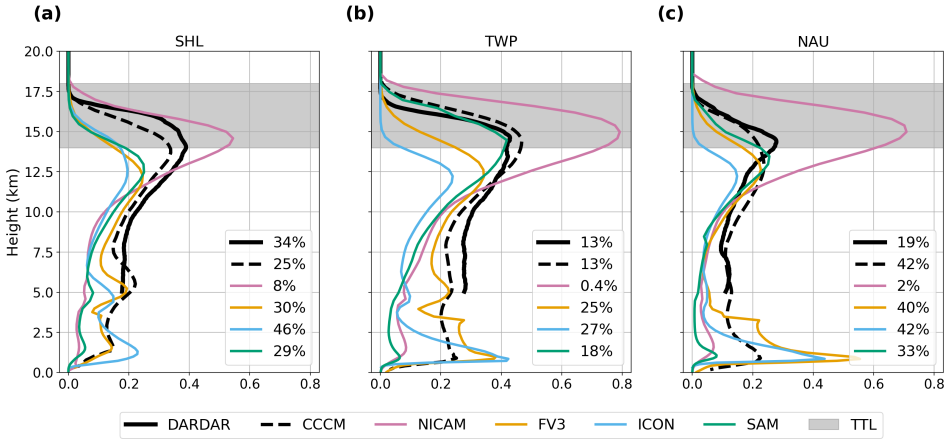

Figure 10. Same as Figure 6 but for the (a) SHL, (b) TWP, and (c) NAU. The radar-lidar product from CCCM shows the combined liquid and ice-phase cloud occurrence. The clear-sky percentages are noted in the legend for SHL, TWP, and NAU, respectively.

4.2 Vertical Structure of Clouds

In the CCCM and DARDAR observations, all regions have a primary peak in cloud occurrence near the base of the TTL (Figure 10b). The TWP has the highest cloud occurrence at all heights (Figure 10b) and the most cloud cover (time-area percentage of cloudy columns) at nearly 87%. The SHL (Figure 10a) has comparable vertical cloud occurrence in the TTL but much less column cloud cover (66% in DARDAR and 75% in CCCM). DARDAR also shows a stronger trimodal peak in cloud occurrence in the SHL, as noted by Johnson et al. (1999). Fewer TTL and mid-troposphere clouds as well as a weaker peak in cloud occurrence at the freezing level in NAU indicate weaker or less frequent deep convection (Figure 10c). FV3, ICON, and SAM reproduce the trimodal distribution of clouds in the SHL, but fail to simulate enough TTL clouds. In all regions, NICAM overestimates the cloud occurrence in the TTL and underestimates clouds in the lower troposphere.

The models have characteristic biases in the vertical structure of clouds that are fairly similar in the SHL and NAU to the TWP and correlate well with the model differences in the joint albedo-OLR histogram. Compared to the TWP, each model simulates fewer TTL and mid-troposphere clouds in NAU consistent with observations and the TOA radiative fluxes shown in the joint albedo-OLR histograms (Figure 4). ICON has the lowest cloud-top heights and correspondingly few instances of low OLR values. The population of low clouds in FV3 shows up in the vertical occurrence as a strong peak in boundary layer and intermediary clouds near the freezing level. The joint histogram of NICAM does not visually capture the high occurrence of clouds in the TTL. The low occurrence of deep convection in SAM is not apparent in the vertical occurrence; hence, the properties of clouds in SAM need to be further examined.

4.3 FWP Categorization

The FWP histograms for the TWP for the DARDAR observations and the four NFIS models from Figure 7a–e are reproduced as the green lines in Figure 11a–e. The FWP histograms for the SHL and NAU are in the orange and purple lines, respectively. The

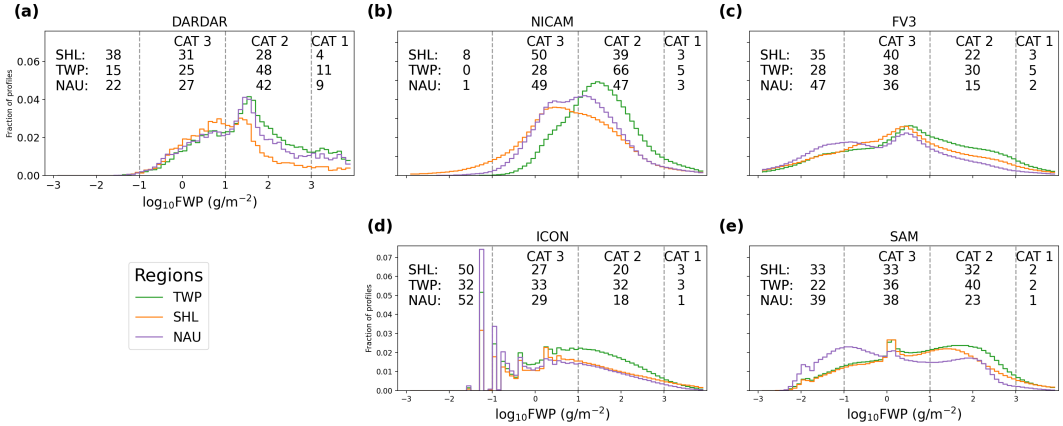

Figure 11. Normalized histograms of total column FWP for the SHL (orange), NAU (purple), and TWP histogram (green; same as black line in Figure 7 histograms) for (a) DARDAR, (b) NICAM, (c) FV3, (d) ICON, and (e) SAM. The categories are divided by vertical dashed lines. Columns with FWP below 0.1 g m^{-2} are considered to be cirrus-free. Listed at the top of each subplot is the percentage of columns from days 3–40 in each region for each category.

fraction of columns in each category is listed above the histograms in each plot. Recall that DARDAR observations are from 2009, which had more precipitation in the TWP and NAU than 2016. This difference should be considered when comparing the observed and simulated FWP histograms.

The DARDAR FWP histogram for the SHL has a similar mode (20–30 g m^{-2}) as for the TWP, but FWPs exceeding this mode are much rarer in the SHL while smaller FWPs are slightly more common. The DARDAR FWP histogram for NAU is similar to the TWP, but with slightly less occurrence at FWPs above the modal value (Figure 11a). Qualitatively similar regional differences are seen in the GSRMs; however, for NICAM and SAM, their modal FWPs also shift downward at the SHL and NAU relative to TWP (Figure 11b, e). The FWP histogram changes more from TWP to NAU in all GSRMs than in DARDAR. The differences between GSRMs are broadly similar in the SHL and NAU as in the TWP.

4.4 Regional Albedo and OLR vs. FWP category

Figure 12 compares the median values of albedo and OLR plane in each FWP category across models and regions. It builds on Figure 8, which presented similar information for the TWP in a complementary form. The models are not coarsened to match CCCM in order to capitalize on the fine resolution of the native grids of the GSRMs. The black line of neutral CRE is only drawn for the TWP region; the line for NAU is nearly identical but the SHL line is at a much higher albedo.

Looking first at Figure 12a, the CCCM data suggest that the OLR and albedo of the thickest (CAT 1) tropical deep convective clouds are similar across regions. Similarly, for the thickest clouds in all NFIS models except SAM, there is generally more intermodel variability in than intra-model regional variability. As we progress to categories with successively smaller FWPs, the opposite occurs, with the CCCM observations and the models generally agreeing on the regional differences in clear-sky albedo and OLR. These regional differences are driven by the higher surface albedo of the SHL and the drier conditions in the SHL and NAU than in the TWP (Figure 12d).

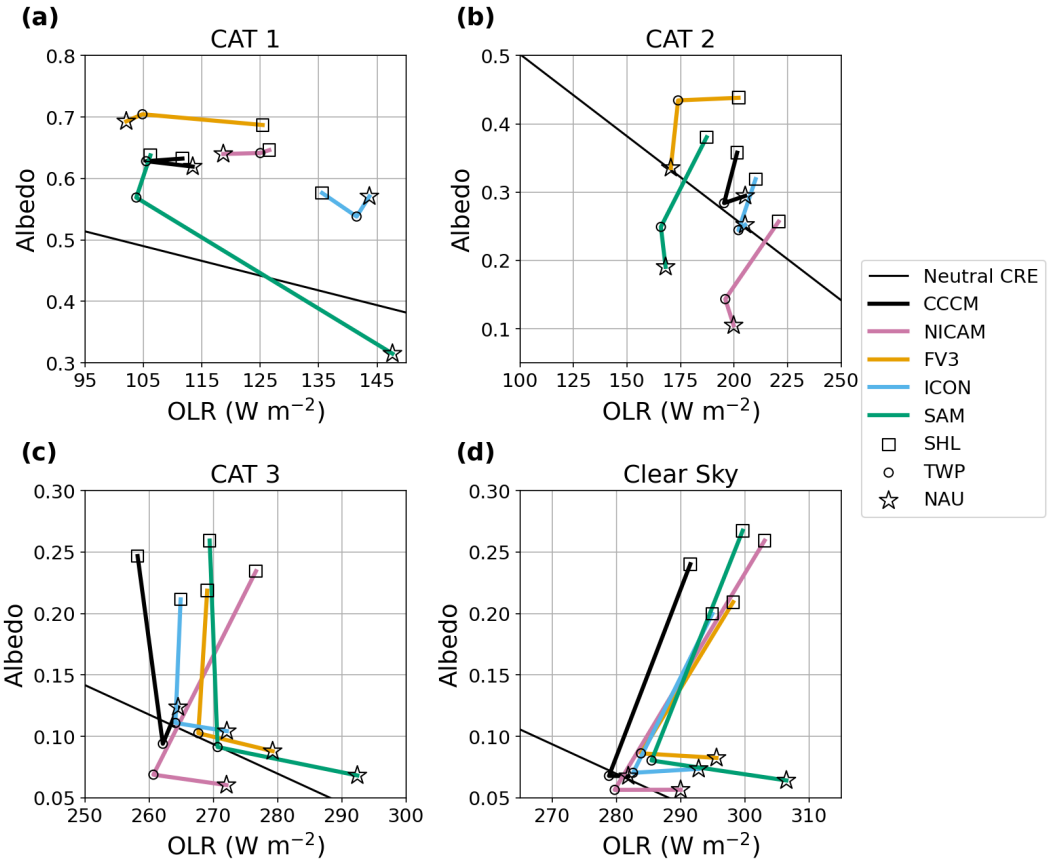

Figure 12. (a) CAT 1, (b) CAT 2, (c) CAT 3, and (d) clear-sky median values for the SHL (square), TWP (circle), and NAU (star) in each model and CCCM. The scale and axis limits are different for CATs 1 and 2. Compared to clear sky, CAT 3 is shifted to lower OLR values by 15 W m^{-2} but has the same x and y scales. The line of neutral CRE calculated from CCCM is shown for the TWP.

In CAT 1 (deep convection, shown in Figure 12a), the models have a diversity of small regional shifts in OLR indicating disagreement on which region has the coldest cloud tops (SHL for ICON; NAU for FV3 and NICAM; and TWP for SAM and the observations). However, consistent with Figure 11 and 9, the differences between models in this category are mostly similar across regions, except for SAM in NAU and FV3 in the SHL.

In CAT 2 (anvil and thick cirrus, shown in Figure 12b), systematic regional differences are seen in both the observations and the models. This FWP category is associated with a higher albedo over the bright underlying surface of the SHL than in the two other ocean regions. The OLR of thick cirrus, through which little longwave radiation can penetrate from below, varies less between regions because its cloud-top temperature is similar across regions.

In CAT 3 (thin cirrus, shown in Figure 12c), regional differences start to dominate model differences. Both in models and observations, the albedos are only slightly higher than the clear-sky values shown in Figure 12d, but the OLRs are reduced about 20 W m^{-2} over the ocean regions and 30 W m^{-2} over the drier SHL region. The bright surface of the SHL dominates the regional albedo variations. Over the ocean, the thin cirrus in ICON often have underlying liquid clouds which give it the largest CAT 3 albedo among the models

and bring it closest to the observed albedo in NAU. Except for NICAM in the TWP, the observed OLR is overestimated in CAT 3 and the clear sky category by all models in all regions.

5 TTL Cirrus

In this section, we investigate a particular subset of cirrus with especially high cloud tops: TTL cirrus. The TTL is the layer of the atmosphere that has properties transitioning between the troposphere and stratosphere, approximately 14–18 km above sea level in the tropics. TTL cirrus are interesting to study because they have a significant impact on water vapor in the TTL and stratosphere (e.g., Virts & Houze, 2015; Holton & Gettelman, 2001). Some TTL cirrus are thick enough to significantly reduce OLR (Fueglistaler et al., 2009).

5.1 Categorization

The TTL IWP was calculated by integrating the 3D cloud ice within the 14–18 km layer for NFIS. Even though NICAM has TTL FWP, we use TTL IWP for consistency between models; the results differ slightly in CAT 1. We use the total frozen condensate (FWP) in the TTL for DARDAR because DARDAR does not differentiate the different hydrometeors. The NICAM hydrometeor profiles in Figure 3 suggest that the missing snow and graupel will mostly affect CAT 1 (deep convection); there is likely minimal impact on CAT 2 or 3.

In Figure 13, the TTL IWP histogram for CAT 1 (green) is plotted on the bottom, with the TTL IWP histograms for CAT 2 (red) and CAT 3 (blue) stacked on top. The black line shows the histogram of the total TTL IWP (FWP for DARDAR). The time-mean frequency of columns in each category that contain TTL cirrus is listed in the legend. A TTL IWP (FWP for DARDAR) threshold of 0.1 g m^{-2} is used to determine the presence of TTL cloud. Columns below this threshold are shaded in gray.

Of the models, NICAM's TTL IWP distribution best matches the shape of DARDAR TTL FWP in each region (Figure 13ii) but is shifted to larger FWPs by an order of magnitude for CATs 2 and 3. That is, NICAM has thicker cirrus in the TTL than observations suggest.

On the other hand, FV3, ICON, and SAM appear to have too little ice in TTL cirrus. These models all have roughly equal proportions of TTL cirrus in CATs 2 and 3. The TTL IWP is smallest in ICON, for which it rarely exceeds 5 g m^{-2} in the TWP or 1 g m^{-2} in the SHL and NAU. Based on Part I, this is likely due to a lack of convection in ICON that is deep enough to reach the TTL. These three models also often generate nonzero ice concentrations in the TTL that are too small to classify as a cloud. Again, the NFIS models look very similar across regions but have different characteristics of ice in the TTL from each other. Like the NFIS FWP modes and category frequencies scatter around observations, so do the NFIS TTL IWP characteristics. We have shown that ICON consistently has too little ice in the TTL and NICAM consistently has too much. SAM matches the category frequencies and the range in FWP and TTL IWP values well.

5.2 Conditional Occurrence of TTL Cirrus vs. Overall FWP Category

The percentages of columns with TTL cirrus are listed in Table 2 for the models and observations in each region. In CAT 1 columns, TTL cirrus typically overlay deep convection that has penetrated the TTL (see Part I). In CAT 2 columns, TTL cirrus may form the top of a thicker ice cloud or overlay other ice cloud layers. CAT 3 columns typically contain one cirrus layer that may lie partly or wholly in the TTL. Table 2 also shows the fraction of columns in which all cloud ice is in TTL cirrus alone; these are mainly a subset of CAT 3.

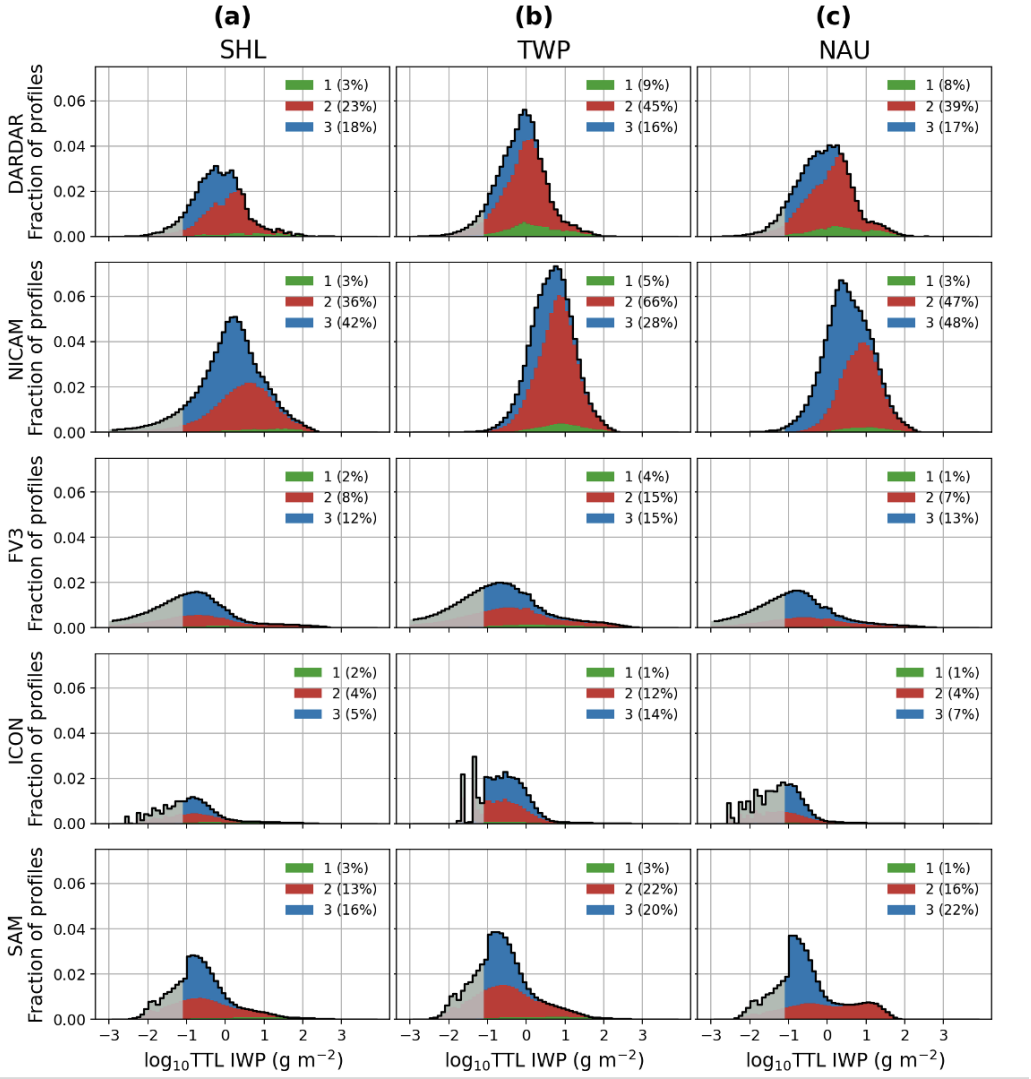

Figure 13. Stacked histograms of the TTL IWP (g m^{-2}) integrated from 14–18km for each total-column FWP category for the models and TTL FWP for DARDAR. CAT 1 (green) indicates the TTL IWP over deep convection; CAT 2 (red) is TTL cirrus above or connected to anvil and is stacked on top of CAT 1; CAT 3 (blue) is stacked on top of CAT 2. The black line shows the total histogram of TTL FWP/IWP.

Taking the TWP as a representative example, CAT 1 has the highest conditional occurrence of ice in the TTL for both observational data (84–88%) and all models (41–100%). This is consistent with the findings from Part I that nearly all of the mass flux of frozen water into the TTL is associated with deep convection. CAT 2 and CAT 3 columns have a somewhat lower conditional occurrence frequency of TTL cirrus. The large disparity between the two observational data, especially for CAT 3, may reflect the more restrictive cloud mask used by DARDAR (Cazenave et al., 2019).

NICAM has too much TTL cirrus conditioned on all three FWP categories, while ICON has too little. FV3 and SAM have plausible TTL cirrus frequency in CAT 1, but too low a TTL cirrus frequency in CATs 2 and 3.

Table 2. Frequency of TTL cirrus for the SHL, TWP, and NAU is shown for each category as a percentage of columns in that category. The frequency of isolated TTL cirrus (i.e., clouds in the TTL but no clouds below the TTL) is shown as a percentage of all columns.

	SHL				TWP				NAU			
	CAT 1	CAT 2	CAT 3	Iso TTL Ci	CAT 1	CAT 2	CAT 3	Iso TTL Ci	CAT 1	CAT 2	CAT 3	Iso TTL Ci
DARDAR	81	74	67	1	84	79	71	1	88	81	73	1
CCCM	71	32	8	3	88	49	22	6	66	24	8	2
NICAM	97	94	86	9	100	100	99	3	100	100	99	11
FV3	80	41	32	2	89	53	40	1	92	59	43	1
ICON	37	21	12	1	41	34	35	3	20	15	15	1
SAM	79	40	46	5	84	53	53	4	85	67	56	7

Note. Iso TTL Ci = Isolated TTL cirrus.

In Table 2, the fourth column for each region shows that isolated TTL cirrus are relatively rare, both in the observations and the GSRMs (except NICAM). The IWP of isolated TTL cirrus is similarly small in FV3, ICON, and SAM (0.27 g m^{-2}, 0.43 g m^{-2}, and 0.51 g m^{-2}, respectively), but NICAM has a mean TTL IWP an order of magnitude larger (3.4 g m^{-2}).

6 Summary and Discussion

We have compared the population of tropical cirrus clouds simulated by the DYAMOND GSRMs with a suite of satellite observations. We focus especially on albedo-OLR joint histograms, since they directly connect to the longwave and shortwave radiative effects of the cloud population. GSRMs explicitly resolve deep convection, the most important cirrus-initiating process, and they also resolve the resulting cirrus clouds, so it is plausible that they will simulate tropical cirrus much more realistically than conventional GCMs.

We use a statistical approach to examine the life cycle of modeled convective systems and cirrus in the DYAMOND GSRMs. Three $10^\circ \times 10^\circ$ latitude-longitude regions in the tropics are used to represent different deep convective regimes: local and remote ocean convection (TWP and NAU) and land convection (SHL).

We interpret the albedo-OLR histograms in terms of an aggregate life cycle of tropical cirrus that begins with convective systems, then transitions through anvils to cirrus with correspondingly smaller frozen water paths. The effect of deep convection on cirrus was investigated in Part I; we pick up from there. After convective injection, each model simulates a path to thin cirrus in the albedo-OLR plane. These paths are different between models in ways that are robust across the three study regions. This is due to inherent model differences in the formulation of microphysics and fine-scale dynamics that influence the typical cirrus height, optical depth, and cloud fractional coverage. As a group, the GSRMs also capture the more subtle differences in the cirrus population between the three study regions.

Many model biases in the albedo-OLR histogram and their overall TOA radiative fluxes can be traced to aspects of their simulation of cirrus clouds. Four GSRMs provided the necessary outputs for this analysis. NICAM has a low mean OLR due to its excessive cirrus extent and high cloud-top heights, but reasonably reproduces the observed cloud populations and captures the regional differences quite well. FV3 has the smallest radiative biases in the 38-day climatology and simulates deep convection well in all three regions. FV3 also consistently produces a population of bright clouds with intermediate OLR that we interpret as congestus mostly composed of liquid water. These liquid-dominated clouds are observed at NAU but not at TWP or SHL. ICON consistently fails to simulate convection and cirrus that are deep enough or cirrus that are extensive enough, leading to excessive OLR. SAM

does not simulate sufficiently optically thick deep convective cores and instead tends to generate thick anvil clouds with low albedo.

The FWP histogram is another revealing and observable metric of ice cloud properties. In GSRMs, this metric is sensitive to the ice microphysics parameterization. The models as a group produce a wide range of FWP distributions with modes and amplitudes that scatter around observed values. Modest regional differences are observed in the FWP histogram. These differences are qualitatively reproduced by the GSRMs, but are much smaller than the tropics-wide differences in the FWP histograms simulated by the four models. The shape of the observed histogram is most closely matched by NICAM, even though NICAM simulates too much cirrus cloud, especially in the TTL.

In the TTL, the models retain aspects of the total column FWP distribution but with the mode shifted to small IWPs ($\sim$0.3 g m^{-2}). While most CAT 1 deep convective columns have ice in the TTL, the majority of TTL cirrus occur in CATs 2 and 3.

One motivation for using GSRMs is to expand our understanding of tropical cirrus by filling in observational gaps, but the models need further improvements to be more useful for studying the physical properties of the TTL and the life cycle of tropical clouds. Improvements for each model could include changes to the model physics, such as improved ice microphysics. In addition, analysis would be enhanced by saving model variables such as full 3D frozen hydrometeor output for radiatively active hydrometeors, optical depths, and clear-sky radiative fluxes to directly compare radiative effects to observations. Nonetheless, GSRMs in the DYAMOND simulations provide an illuminating range of model behavior and simulated TTL cirrus which will only be enhanced by further improvements in model subgrid processes.

Sensitivity studies would help determine how microphysics parameterizations affect the presence and radiative effects of TTL cirrus. Future work could include the role of cirrus in dehydrating the TTL in GSRMs. Simulations of boreal winter from DYAMOND Winter, the second phase of the DYAMOND project, may also provide an interesting contrast to the summer simulations presented here. The GSRMs in both phases of DYAMOND provide ample opportunity for studying the TTL, its properties, and cirrus clouds.

Acknowledgments

DYAMOND data management was provided by the German Climate Computing Center (DKRZ) and supported through the projects ESiWACE and ESiWACE2. The projects ESiWACE and ESiWACE2 have received funding from the European Union's Horizon 2020 research and innovation programme under grant agreements No 675191 and 823988. DARDAR data were obtained from the ICARE Data and Services Center (`http://www.icare.univlille1.fr/projects/dardar`). The satellite data from the A-Train Integrated CALIPSO, CloudSat, CERES, and MODIS Merged Product Release B1 (CCCM) and CERES Synoptic 1-degree product were obtained from the NASA Langley Research Center Atmospheric Science Data Center (`https://doi.org/10.5067/AQUA/CERES/NEWS_CCCM-FM3-MODIS-CAL-CS_L2.RELB1`). The source code for the analysis to this paper can be found on `https://github.com/smturbev/turbeville_2021_lifecycle_paper/`. We thank Adam Sokol and Blaž Gasparini for their insightful discussions. This material is based upon work supported by the National Science Foundation through the Partnerships in International Research and Education program under grant number OISE-1743753. The corresponding author, Turbeville, is an ARCS Foundation Fellow and GO-MAP scholar.

References

Ackerman, T. P., Liou, K.-N., Valero, F., & Pfister, L. (1988). Heating rates in tropical anvils. *J. Atmos. Sci.*, *45*(10), 1606-1623. doi: 10.1175/1520-0469(1988)045⟨1606:HRITA⟩2.0.CO;2

Berry, E., & Mace, G. G. (2014). Cloud properties and radiative effects of the asian summer monsoon derived from a-train data. *Journal of Geophysical Research: Atmospheres*, *119*(15), 9492-9508. doi: 10.1002/2014JD021458

Cazenave, Q., Ceccaldi, M., Delanoë, J., Pelon, J., Groß, S., & Heymsfield, A. (2019). Evolution of dardar-cloud ice cloud retrievals: new parameters and impacts on the retrieved microphysical properties. *Atmospheric Measurement Techniques*, *12*(5), 2819–2835. doi: 10.5194/amt-12-2819-2019

Del Genio, A. (2012). Representing the sensitivity of convective cloud systems to tropospheric humidity in general circulation models. *Surv Geophys*, *33*, 637–656. doi: 10.1007/s10712-011-9148-9

Deng, M., Mace, G. G., Wang, Z., & Lawson, R. P. (2013, 04). Evaluation of Several A-Train Ice Cloud Retrieval Products with In Situ Measurements Collected during the SPARTICUS Campaign. *Journal of Applied Meteorology and Climatology*, *52*(4), 1014-1030. doi: 10.1175/JAMC-D-12-054.1

Fueglistaler, S., Dessler, A. E., Dunkerton, T. J., Folkins, I., Fu, Q., & Mote, P. W. (2009). Tropical tropopause layer. *Rev. Geophys.*, *47*(RG1004). doi: 10.1029/2008RG000267

Gasparini, B., Blossey, P. N., Hartmann, D. L., Lin, G., & Fan, J. (2019). What drives the life cycle of tropical anvil clouds? *Journal of Advances in Modeling Earth Systems*, *11*(8), 2586-2605. doi: 10.1029/2019MS001736

Hartmann, D. L., Moy, L. A., & Fu, Q. (2001). Tropical convection and the energy balance at the top of the atmosphere. *Journal of Climate*, *14*, 4495-4511. doi: 10.1175/1520-0442(2001)014⟨4495:TCATEB⟩2.0.CO;2

Hartmann, D. L., & Short, D. A. (1980, 06). On the Use of Earth Radiation Budget Statistics for Studies of Clouds and Climate. *Journal of the Atmospheric Sciences*, *37*(6), 1233-1250. doi: 10.1175/1520-0469(1980)037⟨1233:OTUOER⟩2.0.CO;2

Hollars, S., Fu, Q., Comstock, J., & Ackerman, T. (2004). Comparison of cloud-top height retrievals from ground-based 35 ghz mmcr and gms-5 satellite observations at arm twp manus site. *Atmospheric Research*, *72*(1), 169-186. (Clouds and Radiation) doi: 10.1016/j.atmosres.2004.03.015

Holton, J. R., & Gettelman, A. (2001). Horizontal transport and the dehydration of the stratosphere. *Geophysical Research Letters*, *28*(14), 2799-2802. doi: 10.1029/2001GL013148

Houze, R. A. (1981). Cloud clusters in large-scale vertical motions in the tropics. *Journal of the Meteorological Society of Japan*, *60*(1), 396-410. doi: 10.2151/jmsj1965.60.1_396

Inoue, T., Satoh, M., Hagihara, Y., Miura, H., & Schmetz, J. (2010). Comparison of high-level clouds represented in a global cloud system–resolving model with calipso/cloudsat and geostationary satellite observations. *Journal of Geophysical Research: Atmospheres*, *115*(D4). doi: 10.1029/2009JD012371

Johnson, R. H., Rickenbach, T. M., Rutledge, S. A., Ciesielski, P. E., & Schubert, W. H. (1999, 08). Trimodal Characteristics of Tropical Convection. *Journal of Climate*, *12*(8), 2397-2418. doi: 10.1175/1520-0442(1999)012⟨2397:TCOTC⟩2.0.CO;2

Kato, S., Rose, F. G., Rutan, D. A., Thorsen, T. J., Loeb, N. G., Doelling, D. R., ... Ham, S.-H. (2018, 05). Surface Irradiances of Edition 4.0 Clouds and the Earth's Radiant Energy System (CERES) Energy Balanced and Filled (EBAF) Data Product. *Journal of Climate*, *31*(11), 4501-4527. doi: 10.1175/JCLI-D-17-0523.1

Kato, S., Rose, F. G., Sun-Mack, S., Miller, W. F., Chen, Y., Rutan, D. A., ... Collins, W. D. (2011). Improvements of top-of-atmosphere and surface irradiance computations with calipso-, cloudsat-, and modis-derived cloud and aerosol

properties. *Journal of Geophysical Research: Atmospheres*, *116*(D19). doi: https://doi.org/10.1029/2011JD016050

Kiehl, J. T. (1994). On the observed near cancellation between longwave and shortwave cloud forcing in tropical regions. *Journal of Climate*, *7*(4), 559-565. doi: 10.1175/1520-0442(1994)007⟨0559:OTONCB⟩2.0.CO;2

Nugent, J. M., Turbeville, S. M., Bretherton, C. S., Blossey, P. N., & Ackerman, T. P. (2021). *Tropical cirrus in global storm-resolving models. part i: Role of deep convection.* (Unpublished manuscript)

Ramanathan, V., Cess, R. D., Harrison, E. F., Minnis, P., Barkstrom, B. R., Ahmad, E., & Hartmann, D. (1989). Cloud-radiative forcing and climate: Results from the earth radiation budget experiment. *Science*, *243*(4887), 57–63. doi: 10.1126/science.243.4887.57

Sokol, A., & Hartmann, D. (2020). Tropical anvil clouds: Radiative driving towards a preferred state. *JGR: Atmospheres*. doi: 10.1029/2020JD033107

Stephens, G. (2005). Cloud feedbacks in the climate system: A critical review. *Journal of Climate*, *18*(2), 237-273. doi: 10.1175/JCLI-3243.1

Virts, K. S., & Houze, R. A. (2015). Clouds and water vapor in the tropical tropopause transition layer over mesoscale convective systems. *Journal of the Atmospheric Sciences*, *72*(12), 4739 - 4753. doi: 10.1175/JAS-D-15-0122.1

Virts, K. S., Wallace, J. M., Fu, Q., & Ackerman, T. P. (2010, 10). Tropical Tropopause Transition Layer Cirrus as Represented by CALIPSO Lidar Observations. *Journal of the Atmospheric Sciences*, *67*(10), 3113-3129. doi: 10.1175/2010JAS3412.1

Wall, C. J., Hartmann, D. L., Thieman, M. M., Smith, J., William L., & Minnis, P. (2018, 11). The Life Cycle of Anvil Clouds and the Top-of-Atmosphere Radiation Balance over the Tropical West Pacific. *Journal of Climate*, *31*(24), 10059-10080. doi: 10.1175/JCLI-D-18-0154.1